Supplemental Material for:

"Absence of the liquid–liquid transition in aqueous ionic liquids"

Johannes Bachler, Lilli-Ruth Fidler, Thomas Loerting*

Institute of Physical Chemistry, University of Innsbruck, Innrain 52c, A-6020 Innsbruck, Austria

This file consists of detailed experimental procedures and methods as well as additional data that help understanding the conclusions of the main manuscript. It is structured as follows:

Table of Contents

Experimental section 1
Dilatometry 2
X-ray Diffraction 2
Differential Scanning Calorimetry 2
Cryo-Microscopy 3
Conjectured behavior of ideal aqueous solutions using the LLCP scenario 3
Non-ideality of mixtures 4
pH estimates 4
Structural properties of liquid solutions 4
DSC features and reversibility of the transition 5
Assignment of Bragg peaks in the mixtures 6
Full DSC scans of all employed compositions in the water- and solute-dominated region 8
XRD scans of solutions in the solute-dominated region in the full temperature range 9
References ..... **Error! Bookmark not defined.**

Experimental section

Materials and methods

$N_2H_4 \cdot H_2O$ and trifluoroacetic acid (TFA) were purchased from Sigma Aldrich and used without further purification. Solutions are prepared by weighing the components in glass vials that were previously flushed with argon. $N_2H_4 \cdot H_2O$ is first diluted with water (taking into account the water present due to the hydrazine hydrate) after which acid is added slowly to ensure that the solution always stays close to room temperature. Samples are sealed and handled under exclusion of air. Identical procedures are applied for other solutions.

For X-ray diffraction (XRD) as seen in Figure 1A and dilatometry experiments as seen in Figure 2, Hydrazinium trifluoroacetate solutions are quenched to 77 K with cooling rates between 100 and 1000 K/min. For solutions with mole fractions $x>0.13$, this is enough to yield a transparent glassy state. The cooling process is investigated using differential scanning calorimetry (DSC) as displayed in Figure 3A. The sample is either subsequently characterized (see X-ray diffraction) or compressed to 1.8 GPa

at 77 K (see Dilatometry). It was shown that amorphous water can be trapped in a kinetically arrested state at T<100 K ("quench recovery") [32]. Consequently, also these compressed samples are recovered at 77 K and characterized *ex situ* using XRD (Figure 1B) and DSC (Figure 3B). Procedures for dilatometry [22,26], X-ray [33], DSC [34] and microscopy experiments [35] are similar to the ones used reproducibly in earlier work.

Dilatometry

600 μL of each solution are pipetted into an indium container kept at 77 K, which is then sealed manually by deforming the circular opening. Indium is necessary to avoid frictional heating that is triggered by sudden pressure drops. The container is placed in the 8 mm bore of a steel piston cylinder setup (also kept at 77 K). After compression, the samples are brought back to ambient pressure and removed from the steel cylinder, all while remaining at liquid nitrogen temperature. Pressures up to 1.8 GPa are applied vertically using a material testing machine by Zwick Roell (model BZ100/TL3S). The machine is both capable of recording the force and the position of the piston with an accuracy of ±0.5 μm and a spatial resolution of 0.01 μm. This allows *in situ* monitoring of the density/volume changes of the sample. Densification Δd of the samples after compression is evaluated by subtracting the piston displacement in a blind experiment (dotted lines in Figure 2A) at 1.0 GPa (d_0) from the piston displacement observed in Figure 2A at 1.0 GPa ($d_{1.0}$). In other words, Δd displayed in Figure 2B corresponds to the permanent densification of sample alone. The validity of this process will be demonstrated based on the well-known pressure-induced amorphization of ice I to HDA. 600 μL water, which weigh roughly 600 mg at room temperature, crystallize to ice with a density of 0.917 g/cm^3. The volume of ice inside the bore thus corresponds to 0.654 cm^3. As the bore has a diameter of 8 mm, the height of the ice cylinder inside is roughly 13 mm. Upon compression to HDA, the density increases by approximately 25% (from 0.917 to 1.17 g/cm^3). Hence, we would expect to yield 0.513 cm^3 of HDA, or a cylinder of about 10 mm height. This is fully consistent with the value of 3 mm (=13mm-10mm) for Δd shown in Figure 2B.

X-ray Diffraction

Characterization via diffraction is done *ex situ* at ambient pressure on a commercial D8 Bruker Advance X-ray diffractometer equipped with a low-temperature FMB Oxford chamber and a two-stage helium cryostat. The X-ray source with incident wavelength λ=1.54178 A (CuKα) and the detector are set up in 2θ geometry. A Goebel mirror prevents distortion of Bragg reflections. Finely powdered sample is transferred onto the sample holder made of nickel-plated copper precooled to ≈80 K. The chamber is evacuated and diffractograms are recorded in steps upon heating where the individual temperatures are reached with 6 K/min. Scans are performed between 80 and 210 K, with each measurement consuming about 20 minutes. These variable slow heating rates lead to somewhat lower transition temperatures that have been estimated to be ≈10-20 K lower compared to calorimetry using the cold-crystallization temperature of vitrified aqueous ethylene glycol solution [36] and the transition temperatures of pure high-density amorphous ice [28].

Differential Scanning Calorimetry

The thermal behavior of samples is studied *ex situ* using a DSC 8000 by Perkin Elmer with heating/cooling rates of 30 K/min (unless stated otherwise). The instrument has been carefully calibrated using the sharp transition temperatures of cyclopentane, adamantane and indium. Cooling scans as displayed in Figure 3A are obtained by weighing liquid solution at room temperature (≈40 mg) in an aluminum crucible that is sealed airtight and loaded into the instrument.

Characterization of high-pressure samples is carried out by loading about 10 mg into an aluminum crucible at 77 K, which is then transferred into the precooled instrument. The samples are heated from

93 K to 300 K, cooled to 93 K and then reheated again. The cooling scan is used for comparison with samples loaded at ambient temperature. The second heating scan serves as a baseline and helps to identify irreversible effects. Since we are unable to weigh these samples while being immersed in liquid nitrogen, we utilize the transition enthalpies for determination of the mass loaded into the crucible. That is, we have first measured the melting enthalpies of cold-loaded solutions and then normalized them based on the latent heat taken up by the samples loaded at ambient temperature.

Cryo-Microscopy

We employ an optical microscope BX-51 (Olympus Corporation, Japan) equipped with a Linkam cryostage LTS420 that allows reaching temperatures as low as 93 K with controlled rates. A droplet of solution is placed on the object plate and quickly covered in order to avoid evaporation of the droplet and condensation of water vapor of the surrounding atmosphere. Pictures are taken after the solutions were quenched with 40 K/min (the fastest possible rate the stage can reach) to 93 K.

Conjectured behavior of ideal aqueous solutions using the LLCP scenario

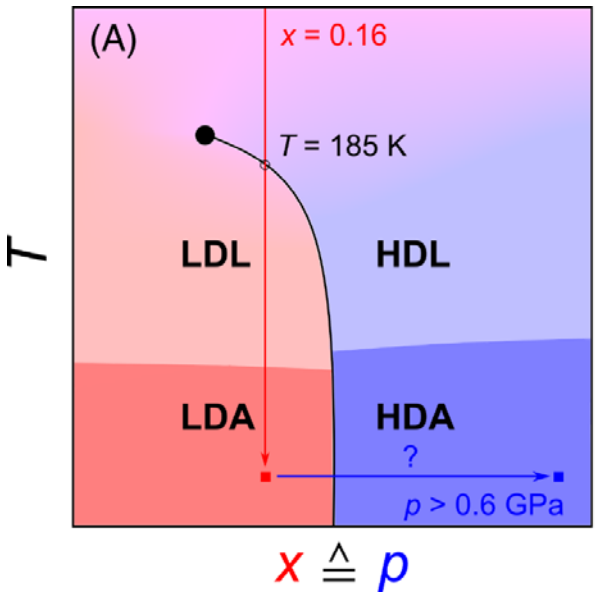

Figure S1. Non-crystalline state diagram of water in the framework of the LLCP scenario. The filled black circle represents the LLCP below which water may be encountered as LDL, HDL or their glassy states. The line emanating from the LLCP indicates the first-order LLPT and traces down to very low temperatures where the first-order like transition between LDA and HDA is found. The red line depicts the route purported by Angell and co-workers assuming that the mole fraction of x=0.156 in their ideal mixture of aqueous $N_2H_5^+TFA^-$ is equivalent to a pressure of 0.15-0.20 GPa. That is, the solution experiences the first-order transition at 185 K attributed to an LLPT of HDL to LDL (black open circle) followed by a glass transition to LDA upon cooling. The transition can be completely reversed upon heating (following the red arrow to higher temperatures. The blue line indicates one of our key experiments to counter this hypothesis, namely the absence of the LDA → HDA transition upon pressurization at low temperatures that would be implied in this scenario [12,13]. The figure has been adapted from ref. [37].

Non-ideality of mixtures

pH estimates

$N_2H_5^+TFA^-$ solutions are produced by simple acid-base neutralization with hydrazine being protonated fully by trifluoroacetic acid. The equilibrium constant for this reaction is on the side of $N_2H_5^+TFA^-$ as TFA is a strong acid. This changes upon adding water which is itself an ampholyte, i.e., it may either donate or accept protons. The equilibrium constant towards protonation of TFA^- is still negligible small due to the vastly different pK_a (14 for H_2O vs. 0 for TFA). That is, most TFA^- will remain deprotonated in solution. However, water accepting protons from hydrazinium is well within reach:

$$N_2H_5^+ + H_2O \leftrightarrow N_2H_4 + H_3O^+ \qquad pK_a=8.1$$

In order to rate the acidity or basicity of aqueous solutions, the pH value is commonly used. The pH is defined as the negative logarithmic (base 10) concentration of H_3O^+ in solution. In one liter of pure water 10^{-7} mol of H_3O^+ are found, which results in the neutral pH of 7. Once the amount of H_3O^+ is known for the respective volume of solution, the pH can be assessed. A $N_2H_5^+TFA^-$ solution with x=0.16 is made by adding roughly 10 mol (1.6 kg) ionic liquid to a liter (1 kg) of pure water. At 25 °C water and hydrazine have about the same density of 1 g/cm^3 whereas trifluoroacetic acid locks in around 1.5 g/cm^3. Consequently, it is safe to assume that their solutions all have densities between 1 and 1.5 g/cm^3. That is, 2.6 kg of solution correspond to a volume between 1.3 and 2.6 L. Solving the simple equation for the acid-base equilibrium of weak acids, we obtain concentrations between 0.00017 (for 2.6 L solution) and 0.00025 mol/L (for 1.3 L solution) H_3O^+. This corresponds to a pH between 3.61 and 3.76, i.e., the solution is about four orders of magnitude more acidic than pure water. This is important because, water clusters with excess protons are structurally distinct from the predominantly tetrahedral geometries encountered in bulk water (see, e.g., ref. [38] and references therein).

We note that this calculation is a simple estimate as ion activity is neglected entirely. However, our main message is that the solutions investigated here are far from ideal. If activity were important, the mixture would also not be ideal by definition.

Structural properties of liquid solutions

Figure S2 reports the dependence of the X-ray pattern of the liquid at 300 K on molar fraction. These scans were recorded in order to counter the claim of ideal mixing. Ideal mixing with water necessitates identical water–water, water–solute, and solute–solute interactions. It is expected that such interactions manifest in similar structural features, i.e., a broad halo peak around 2θ=26° just like in pure water. This is however, not the case and instead a double halo peak emerges around x=0.10, which gets even more pronounced with increasing mole fraction. The composition of x=0.10 could thus also be used to mark the switch from the water-dominated to the solute-dominated region that was suggested in the main manuscript.

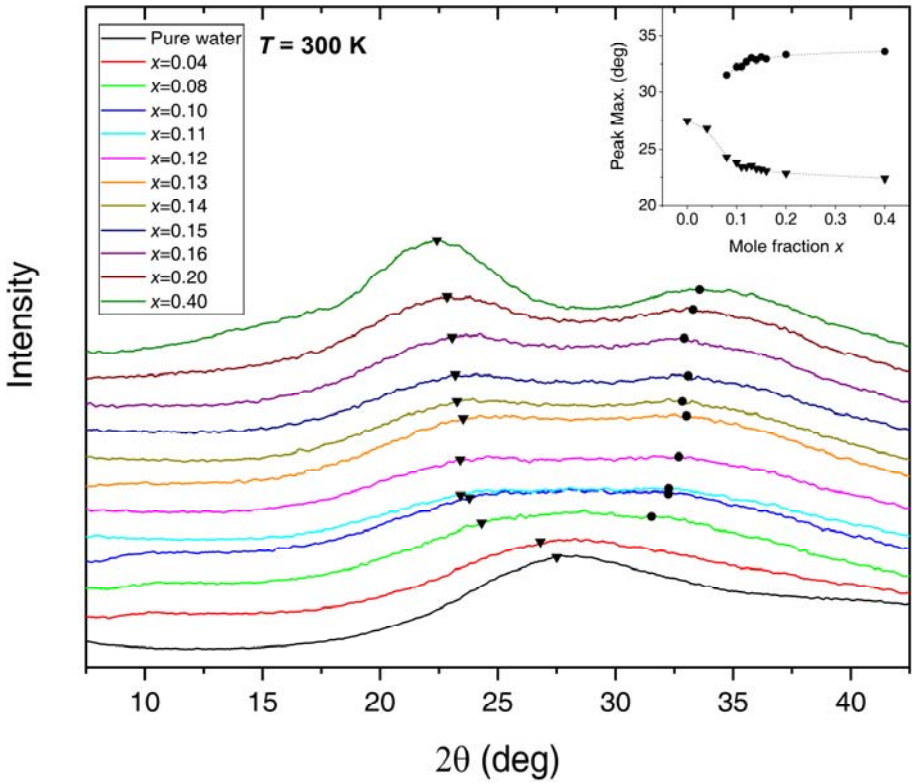

Figure S2. X-ray diffractograms of aqueous $N_2H_5^+TFA^-$ solutions in the liquid state at 300 K. Scans are vertically shifted for clarity and slightly smoothed using adjacent-averaging over 10 points. Triangles and circles represent the peak maxima of the first and second halo, respectively. The maxima are obtained by single Gaussian fits and their position is plotted as a function of mole fraction in the inset.

DSC features and reversibility of the transition

Whether a transition in the deeply supercooled or amorphous regime is reversible or not is highly dependent on the time scale and size of samples. Since we are studying rather large sample amounts using slow heating rates in our XRD instrument, it could be that preemptive crystallization of ice prevents observing the LLPT that was purported by Woutersen et al. [13] using heating rates of about 7 K/min. Figure S3 shows that even with heating rates as low as 1 K/min the transition is reversible, i.e., the endothermic transition necessarily occurs before crystallization.

The endothermic transition is followed by ice and TFA-hydrate crystallization (see also Figure S4). Around 260 K, two melting peaks appear where the first one can be assigned to melting of TFA-hydrate and the second one to melting of ice in liquid solution. The latter is asymmetrical in shape due to continuous dilution of the solution that gradually shifts its melting temperature to higher values. Figure S3 also shows important fundamental characteristics of calorimetry: The heat flow, i.e., the signal intensity, decreases with decreasing rates. On the other hand, the widths of the transitions become narrower. The same holds true when varying the sample mass where a greater amount of sample leads to more intense but also broader signals. In other words, by using large sample amounts of sample and high rates, one trades in narrower signals for better signal intensities. In the case of our samples loaded at ambient temperature, we employ quite large amounts (40 mg) and large rates (30

K/min) that lead to significantly wider peaks. This is also the reason why the endpoint of the transitions are delayed and the mixture needs to be heated to ≈280 K to thaw completely in Figure S3.

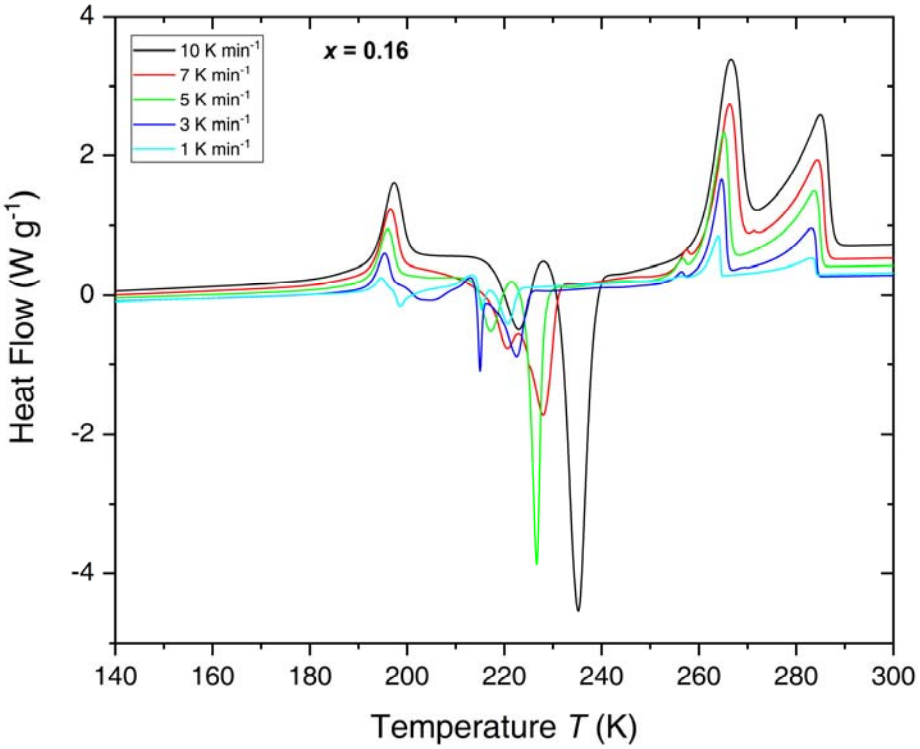

Figure S3. DSC reheating scans of aqueous $N_2H_5^+TFA^-$ solutions with x=0.16 and various (slow) heating rates. All samples were loaded at ambient temperature and vitrified by cooling to 93 K with 50 K/min. The endothermic transition discussed in the main paper appears around 190 K for every heating rate studied.

Assignment of Bragg peaks in the mixtures

Figure 1 in the main manuscript and Figures S7-S16 show that reheating of vitrified concentrated $N_2H_5^+TFA^-$ solutions leads to a variety of complex crystallization products. Identification of the individual components in these mixtures is crucial to understand the phase behavior. Hexagonal ice I is readily identified thanks to its well-known Bragg reflections (see, e.g., Figure 2 in Ref. [33]). Also the reflections of TFA·4H_2O and TFA·H_2O are known [40]. We follow the protocol of Ref. [40] in order to reproduce these results on our instrument. That is, we quench a TFA–H_2O solution with x=0.16 in liquid nitrogen and crystallize it by heating to 200 K before recording diffractograms at 80 K (red line in Figure S4). According to Ref. [40] this yields mixtures of TFA·4H_2O and ice I. Bragg peaks not corresponding to ice I are thus assigned to TFA·4H_2O. As a control, we have also employed a TFA–H_2O solution with x=0.30, which is expected to cold-crystallize to mostly TFA·H_2O (green line in Figure S4).

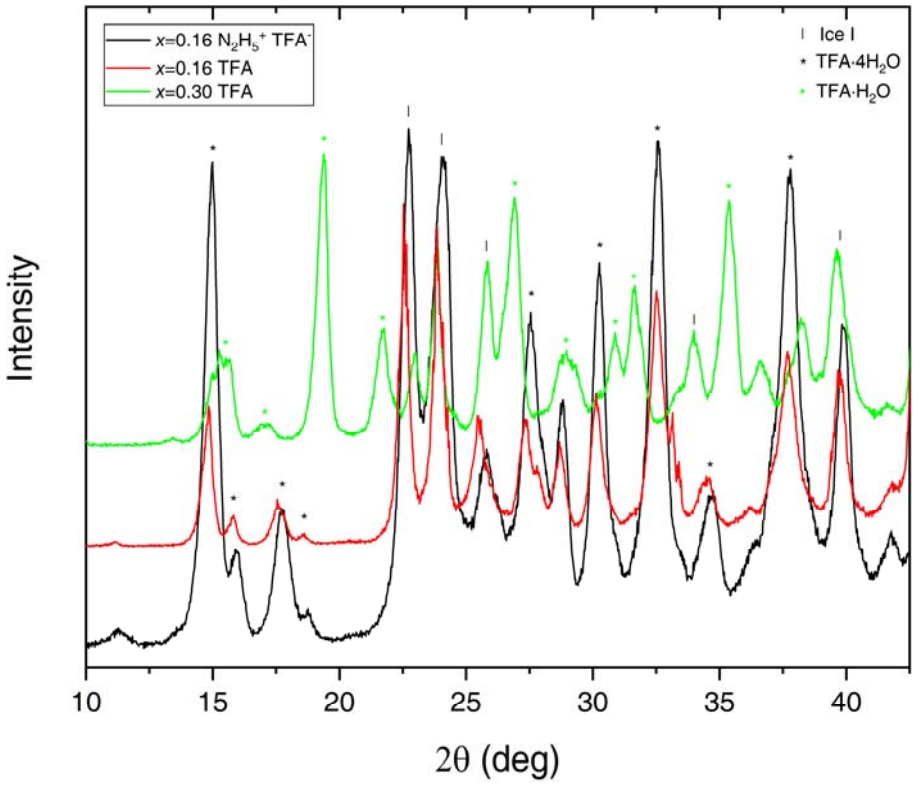

Figure S4. X-ray scans of aqueous $N_2H_5^+TFA^-$ with x=0.16, TFA–H_2O with x=0.16 and TFA–H_2O with x=0.30. Scans are shifted vertically for clarity.

Inspecting the crystallization products of the crystallized $N_2H_5^+TFA^-$ solution with x=0.16 (black line in Figure S4) we find that the Bragg peaks match very well with the ones of the crystallized TFA solution with x=0.16 whereas the crystallized TFA solution with x=0.30 shows a different pattern. We note however, that there is a slight difference in diffractograms of crystallized aqueous $N_2H_5^+TFA^-$ and TFA around 20-30°. This is most likely due to the presence of remaining amorphous hydrazine–water solution resulting in a broad halo peak beneath the sharp Bragg reflections of ice and TFA-hydrate.

Full DSC scans of all employed compositions in the water- and solute-dominated region

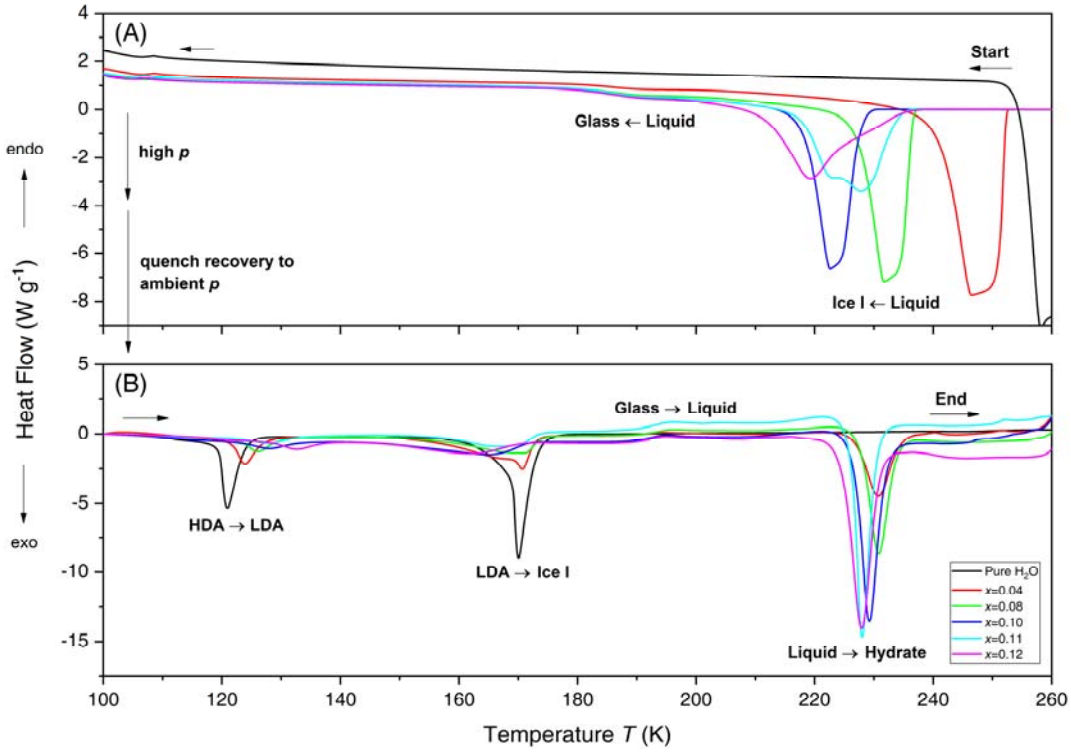

Figure S5: DSC traces (30 K/min) of $N_2H_5^+TFA^-$–water solutions in the water-dominated region at the indicated mole fractions *x*. (**A**) Cooling scans at ambient pressure and (**B**) heating scans of recovered samples after pressurization to 1.8 GPa at 80 K. Curves are normalized by weight of solution and aligned.

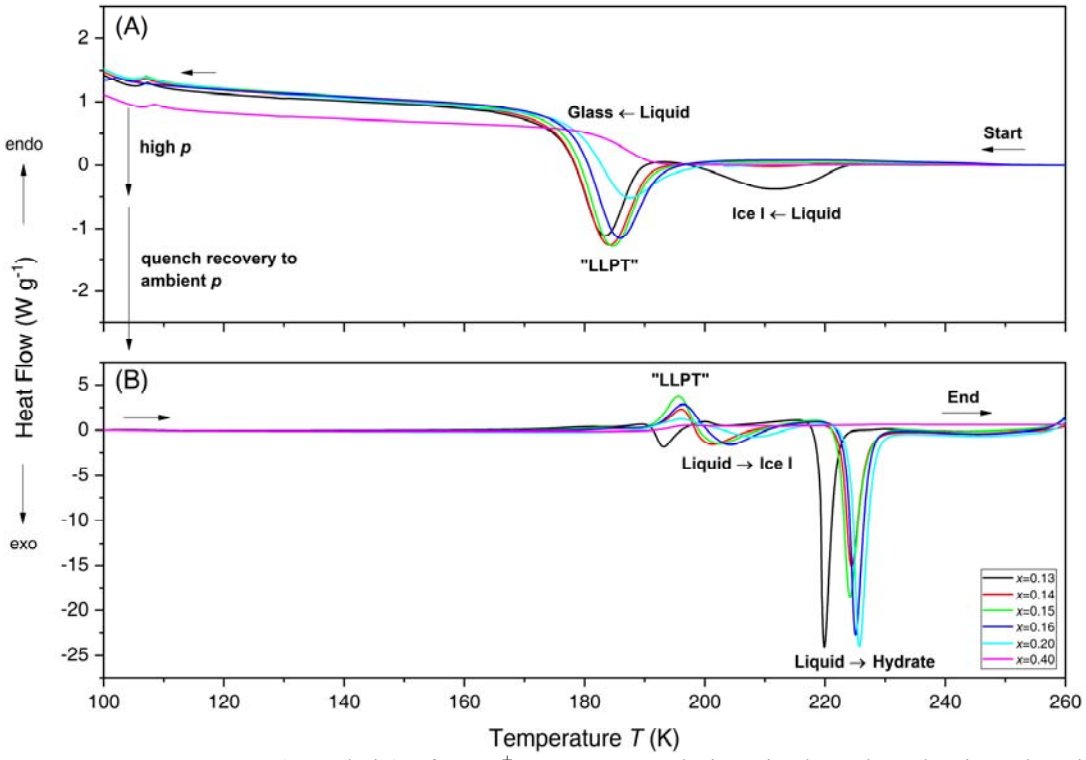

Figure S6: DSC traces (30 K/min) of $N_2H_5^+TFA^-$–water solutions in the solute-dominated region at the indicated mole fractions *x*. (**A**) Cooling scans at ambient pressure and (**B**) heating scans of recovered samples after pressurization to 1.8 GPa at 80 K. Curves are normalized by weight of solution and aligned.

XRD scans of solutions in the solute-dominated region in the full temperature range

While solutions with x=0.16 show no structural evidence for water polyamorphism, this is not straightforward for solutions at $0.13 \leq x < 0.16$ – after all they can clearly be permanently densified. A reasonable explanation for this densification without relying on polyamorphism is offered in the work of Suzuki and Mishima [41] on LiCl–H_2O. Namely, they demonstrate that vitrified concentrated LiCl solutions show permanent densification, however, it is continuous, not involving fundamental structural differences and highly dependent on the initial glassy state. This is phenomenologically different from the transitions involving LDA and HDA and rather corresponds to structural relaxation. Applied to aqueous $N_2H_5^+TFA^-$, this signifies that the glasses made by simply cooling solutions with $0.13 \leq x < 0.16$ are not well relaxed. Annealing or in our case exerting pressure help them to go towards their structural equilibrium yet without showing distinct structural differences of underlying first-order like transitions.

This is evidenced by Figures S7-S16 that show additional X-ray scans upon heating of vitrified hydrazinium trifluoroacetate solutions at $x \geq 0.14$. These scans clearly demonstrate that the first-order transitions encountered in solutions at $0.14 < x < 0.20$ do not provoke distinct structural differences as in genuine polyamorphic transitions, no matter whether pressurized or not. Pressurized vitrified solutions differ from simply vitrified solutions only in their crystallization temperature of ice I. That is, pressurized samples (or at least their surface layers) tend to crystallize at slightly lower temperatures. Please note that the individual crystallization events in X-ray diffraction data occur about 10-20 K

below the ones in DSC data because of the lower heating rate and surface layers slightly warmer than the bulk sample in contact with the sample holder.

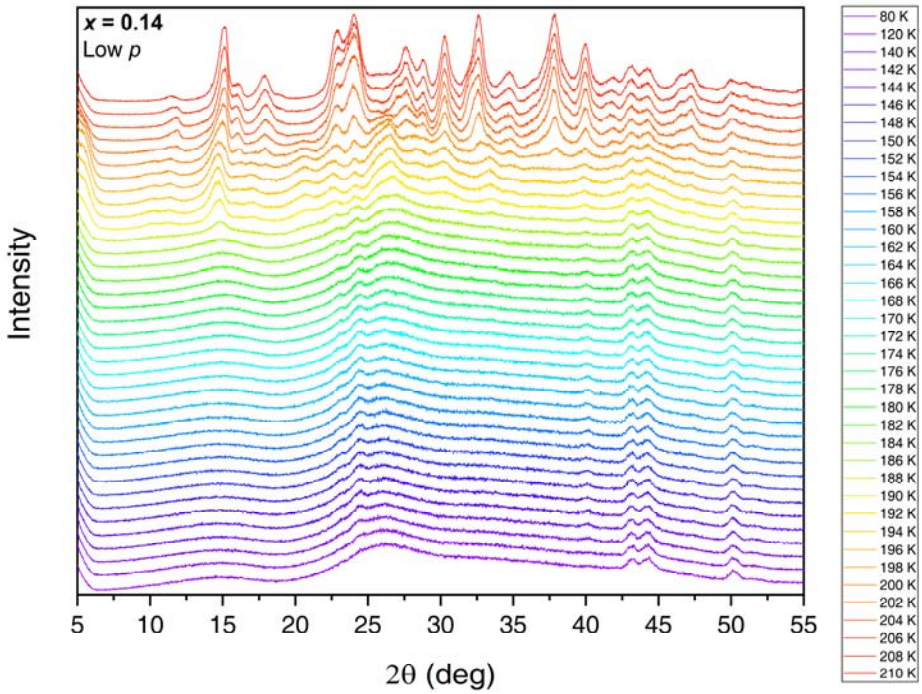

Figure S7: X-ray diffraction patterns of vitrified aqueous $N_2H_5^+TFA^-$ solution (x=0.14) upon heating from 80 K to 210 K. Bragg peaks corresponding to the sample holder are found at 2θ=43, 44, 50°. Scans below 192 K show no sudden jumps of the halo. Weak Bragg peaks of ice in this region testify surface layers warmer than the bulk sample close to the sample holder. Scans above 192 K display the detailed evolution of Bragg peaks (ice I and TFA-hydrate) due to cold-crystallization.

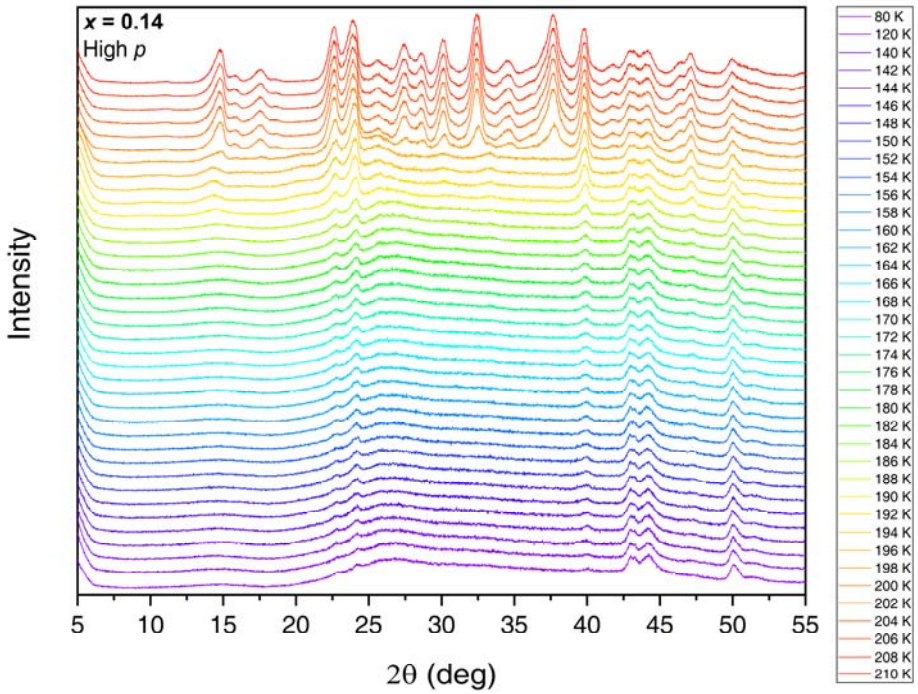

Figure S8: X-ray diffraction patterns at 80-210 K of vitrified aqueous $N_2H_5^+TFA^-$ solution (x=0.14) pressurized to 1.8 GPa. Bragg peaks corresponding to the sample holder are found at 2θ=43, 44, 50°. Just like in simply vitrified solutions, the scans below 192 K show no sudden jumps of the halo peak. Weak Bragg peaks of ice in this region are due to surface layers warmer than the bulk sample close to the sample holder. Scans above 192 K display the detailed evolution of Bragg peaks (ice I and TFA-hydrate) due to cold-crystallization.

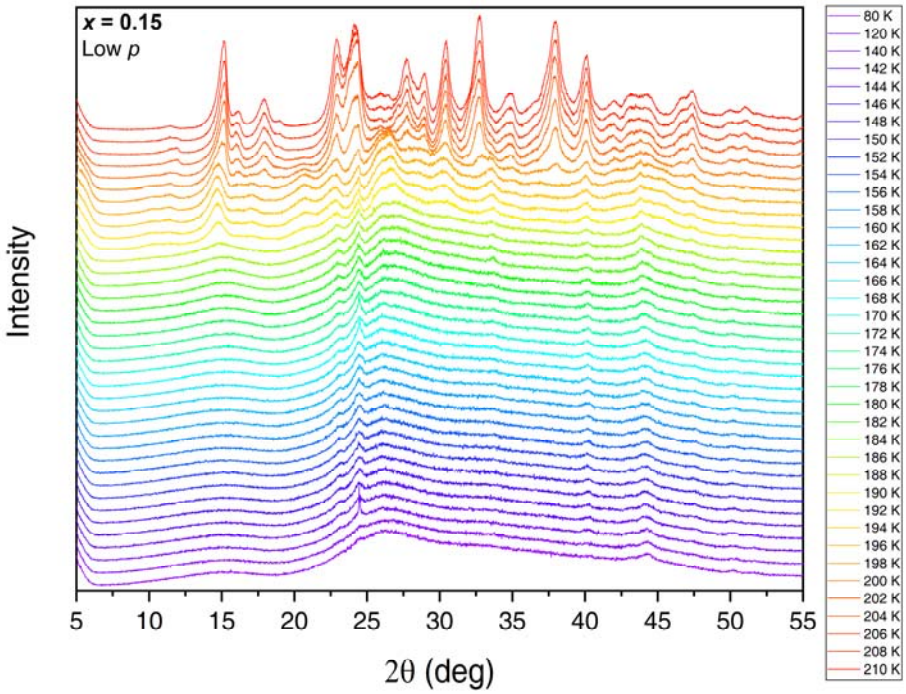

Figure S9: X-ray diffraction patterns of vitrified aqueous $N_2H_5^+TFA^-$ solution (x=0.15) upon heating from 80 K to 210 K. Bragg peaks corresponding to the sample holder are found at 2θ=43, 44, 50°. Scans below 192 K show no sudden jumps of the halo peak. Weak Bragg peaks of ice in this region are due to surface layers warmer than the bulk sample close to the sample holder. Scans above 192 K display the detailed evolution of Bragg peaks (ice I and TFA-hydrate) due to cold-crystallization. At 140 K a spike-like signal is found at 2θ=24°, which is most likely related to an artefact.

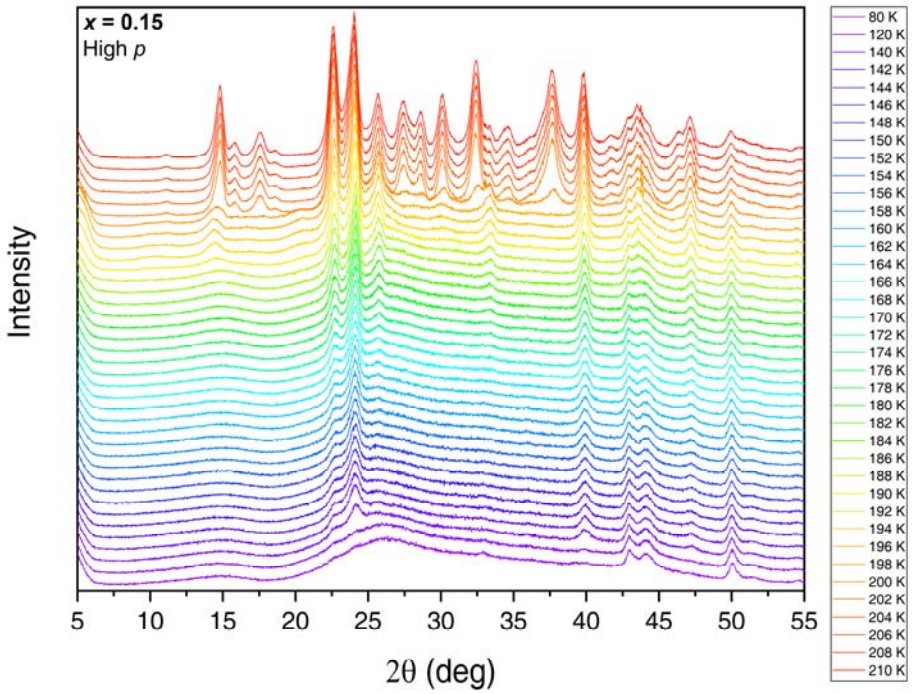

Figure S10: X-ray diffraction patterns at 80-210 K of vitrified aqueous $N_2H_5^+TFA^-$ solution (x=0.15) pressurized to 1.8 GPa. Bragg peaks corresponding to the sample holder are found at 2θ=43, 44, 50°. Accelerated crystallization of ice I (readily identified by the peak at 2θ=40°) at the surface hampers a detailed assessment of the halo peak position here. Scans above 192 K display the detailed evolution of TFA-hydrate Bragg peaks due to cold-crystallization.

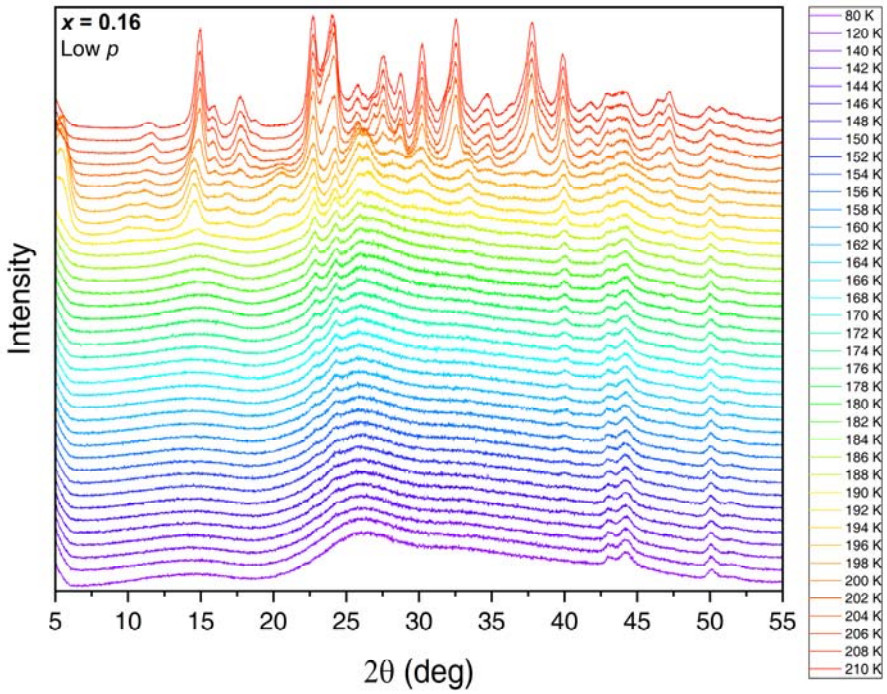

Figure S11: X-ray diffraction patterns of vitrified aqueous $N_2H_5^+TFA^-$ solution (x=0.16) upon heating from 80 K to 210 K. Bragg peaks corresponding to the sample holder are found at 2θ=43, 44, 50°. Scans below 192 K show no sudden jumps of the halo peak. Weak Bragg peaks of ice in this region are due to surface layers warmer than the bulk sample close to the sample holder. Scans above 192 K not discussed in the main manuscript display the detailed evolution of Bragg peaks (ice I and TFA-hydrate) due to cold-crystallization.

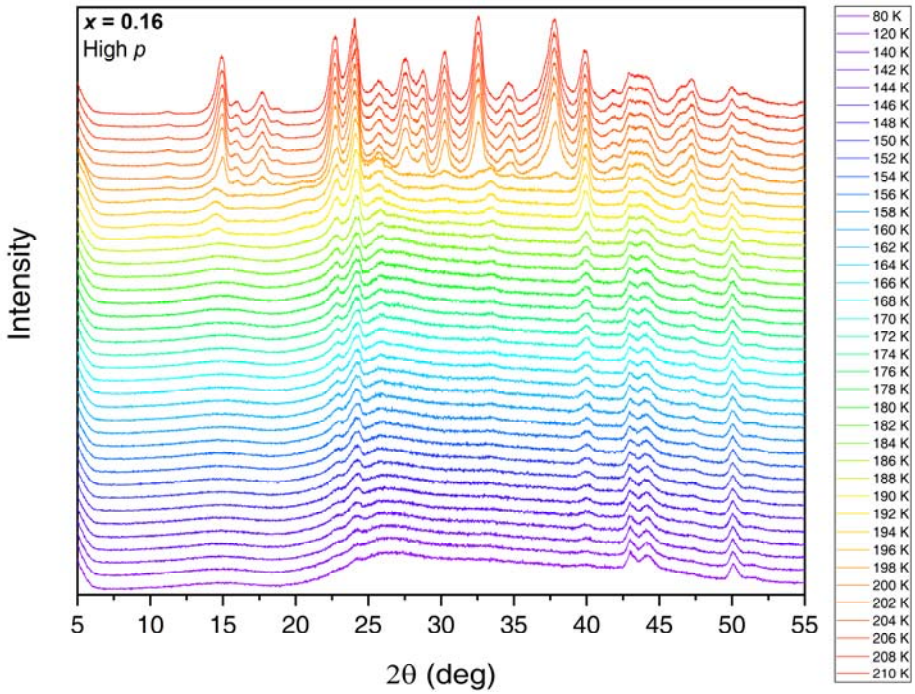

Figure S12: X-ray diffraction patterns at 80-210 K of vitrified aqueous $N_2H_5^+TFA^-$ solution (x=0.16) pressurized to 1.8 GPa. Bragg peaks corresponding to the sample holder are found at 2θ=43, 44, 50°. Scans below 192 K show no sudden jumps of the halo peak. Weak Bragg peaks of ice in this region are due to surface layers warmer than the bulk sample close to the sample holder. Scans above 192 K display the detailed evolution of Bragg peaks (ice I and TFA-hydrate) due to cold-crystallization.

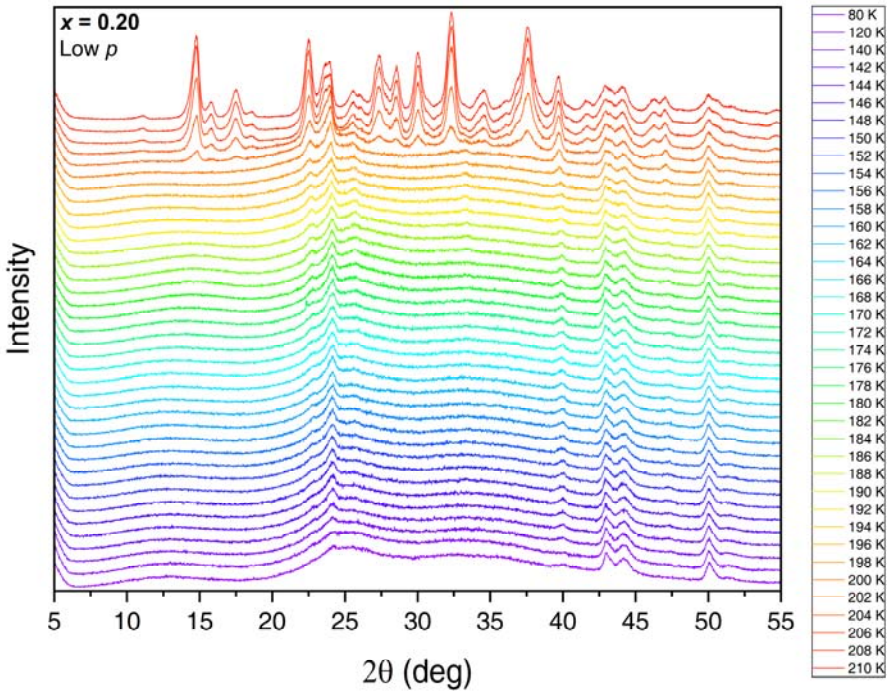

Figure S13: X-ray diffraction patterns of vitrified aqueous $N_2H_5^+TFA^-$ solution (x=0.20) upon heating from 80 K to 210 K. Bragg peaks corresponding to the sample holder are found at 2θ=43,44, 50°. Scans below 192 K show no sudden jumps of the halo peak. Weak Bragg peaks of ice in this region are due to surface layers warmer than the bulk sample close to the sample holder. Scans above 192 K display the detailed evolution of Bragg peaks (ice I and TFA-hydrate) due to cold-crystallization.

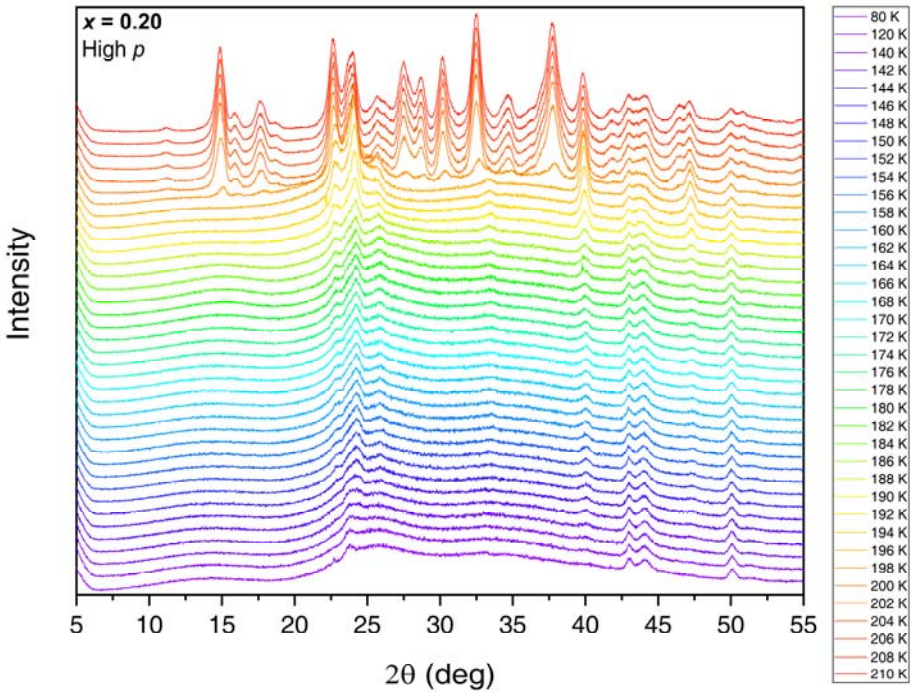

Figure S14: X-ray diffraction patterns at 80-210 K of vitrified aqueous $N_2H_5^+TFA^-$ solution (x=0.20) pressurized to 1.8 GPa. Bragg peaks corresponding to the sample holder are found at 2θ=43, 44, 50°. Accelerated crystallization of ice I (readily identified by the peak at 2θ=40°) at the surface hampers a detailed assessment of the halo peak position here. Scans above 192 K display the detailed evolution of TFA-hydrate Bragg peaks due to cold-crystallization.

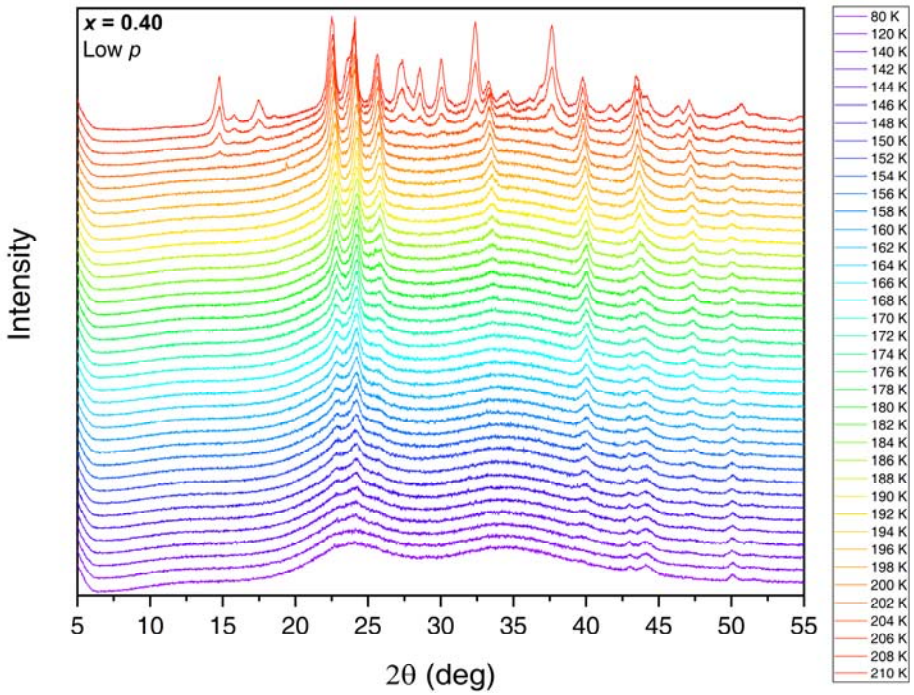

Figure S15: X-ray diffraction patterns of vitrified aqueous $N_2H_5^+TFA^-$ solution (x=0.40) upon heating from 80 K to 210 K. Bragg peaks corresponding to the sample holder are found at 2θ=43,44, 50°. The shoulder at 2θ≈30-40 has evolved into a second halo with a peak maximum of 2θ≈35. Scans below 192 K show no sudden jumps of neither halo peak. Weak Bragg peaks of ice in this region are due to surface layers warmer than the bulk sample close to the sample holder. Scans above 192 K display the detailed evolution of Bragg peaks (ice I and TFA-hydrate) due to cold-crystallization.

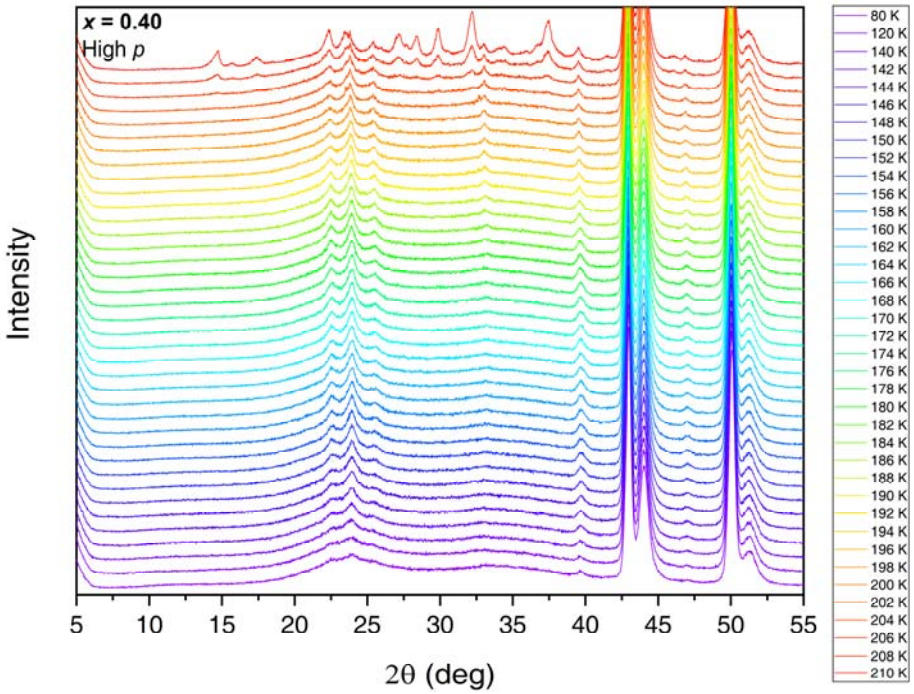

Figure S16: X-ray diffraction patterns at 80-210 K of vitrified aqueous $N_2H_5^+TFA^-$ solution (x=0.40) pressurized to 1.8 GPa. Bragg peaks corresponding to the sample holder are found at 2θ=43, 44, 50°. Accelerated crystallization of ice I (readily identified by the peak at 2θ=40°) at the surface hampers a detailed assessment of the first halo peak position here. The peak position of the second halo however, does not shift significantly with temperature. Scans above 192 K display the detailed evolution of TFA-hydrate Bragg peaks due to cold-crystallization.